Song *et al. Chem Synth* 2023;3:40
DOI: 10.20517/cs.2023.22

Chemical Synthesis

Research Article

Open Access

Check for updates

Deciphering the interaction mechanism between copper and polysulfides for enhanced performance and cost-efficiency in quasi-sodium-sulfur batteries

Haobin Song[1,#], Tong Li[1,#], Tingting He[1], Guanghui Chen[1], Chengjiang Deng[1], Dezhi Kong[2], Dong Yan[3], Hui Ying Yang[4,*], Shaozhuan Huang[1,*]

[1]Key Laboratory of Catalysis and Energy Materials Chemistry of Ministry of Education & Hubei Key Laboratory of Catalysis and Materials Science, South-Central Minzu University, Wuhan 430074, Hubei, China.
[2]Key Laboratory of Material Physics, Ministry of Education, School of Physics and Microelectronics, Zhengzhou University, Zhengzhou 450052, Henan, China.
[3]International Joint Laboratory of New Energy Materials and Devices of Henan Province, School of Physics & Electronics, Henan University, Kaifeng 475004, Henan, China.
[4]Pillar of Engineering Product Development, Singapore University of Technology and Design, Singapore 487372, Singapore.
[#]Authors contributed equally.

Correspondence to: Prof. Shaozhuan Huang, Key Laboratory of Catalysis and Energy Materials Chemistry of Ministry of Education & Hubei Key Laboratory of Catalysis and Materials Science, South-Central Minzu University, Wuhan 430074, Hubei, China. E-mail: husz001@scuec.edu.cn; Prof. Hui Ying Yang, Pillar of Engineering Product Development, Singapore University of Technology and Design, 8 Somapah Road, Singapore 487372, Singapore, E-mail: yanghuiying@sutd.edu.sg

How to cite this article: Song H, Li T, He T, Chen G, Deng C, Kong D, Yan D, Yang HY, Huang S. Deciphering the interaction mechanism between copper and polysulfides for enhanced performance and cost-efficiency in quasi-sodium-sulfur batteries. *Chem Synth* 2023;3:40. https://dx.doi.org/10.20517/cs.2023.22

Received: 26 Apr 2023 **First Decision:** 18 Aug 2023 **Revised:** 31 Aug 2023 **Accepted:** 15 Sep 2023 **Published:** 22 Sep 2023

Academic Editor: Aicheng Chen **Copy Editor:** Yanbing Bai **Production Editor:** Yanbing Bai

Abstract

Room-temperature Na-S batteries with Al current collectors face the long-standing challenges of poor cycling performance and rate capability due to the serious sodium polysulfides (NaPSs) shuttling and sluggish reaction kinetics. Here, we demonstrate that a high-performance and low-cost quasi-Na-S battery can be realized by using the Cu@carbon nanotube (CNT) cathode host and unconventional Cu current collector (Cu-CC) in an ether electrolyte. Detailed *ex-situ* characterizations reveal that the Cu@CNT/S was transformed to NaPSs anchoring on Cu_7S_4 nanocrystals (~11 nm) during the cycling, forming the NaPS@Cu_7S_4/CNT cathode with robust sulfur immobilization and enhanced Na^+ reaction kinetics. Moreover, the chemical interaction between NaPSs and Cu-CC *in situ* creates a robust Cu-CC/electrode interface with ultra-small resistance (< 4 Ω), greatly improving the electrode stability and charge transfer kinetics. The synergy of efficient NaPSs trapping and favorable Cu/electrode interface endows the quasi-Na-S battery with a moderate discharge plateau (around 1.2~1.75 V), excellent rate

© The Author(s) 2023. **Open Access** This article is licensed under a Creative Commons Attribution 4.0 International License (https://creativecommons.org/licenses/by/4.0/), which permits unrestricted use, sharing, adaptation, distribution and reproduction in any medium or format, for any purpose, even commercially, as long as you give appropriate credit to the original author(s) and the source, provide a link to the Creative Commons license, and indicate if changes were made.

capability (396.9 mAh g^{-1} at 10 A g^{-1}), and ultra-stable cycling performance (nearly no capacity decay over 1190 cycles). These features make it quite suitable for stable and cost-sensitive grid-scale applications.

Keywords: Quasi-Na-S battery, copper current collector, Cu/electrode interface, Cu@CNT composite, phase transformation

INTRODUCTION

Room-temperature sodium-sulfur (RT Na-S) batteries are considered one of the most promising battery systems for grid-scale application due to their high energy density (1274 Wh kg^{-1}) and natural abundance of Na and S resources[1-4]. However, RT Na-S batteries face great challenges of low reversible capacity, poor cycling performance, and dissatisfactory rate capability, which impede their practical applications. These problems are mainly triggered by the low conductivity of sulfur and the serious shuttle effect of sodium polysulfides (NaPS), which results in slow redox kinetics and severe active material loss[5]. Moreover, the large volume expansion (~171%) causes electrode collapse and pulverization.

In recent years, various strategies have been proposed to address the abovementioned issues[6,7]. The most common strategy is to incorporate host materials to entrap the sulfur species. Until now, various hollow/porous host materials, such as carbon matrices[8-10], polymer matrices[11], metal sulfides[12-15], metal nitrides[16], *etc.*, have been applied to construct the sulfur cathode. With physical confinement and chemical adsorption, the NaPS shuttling effect is significantly ameliorated. In addition, the separator modification strategy has also been developed to localize the NaPSs on the cathode side and suppress the NaPSs shuttling to the Na metal side[17,18]. The routine cathode/separator modification can improve the performance of RT Na-S batteries; however, they can hardly achieve a long cycle life (> 1,000 cycles) because of the electrode pulverization or final NaPS diffusion to the anode side. Moreover, the design of host/separator materials usually requires complicated nanostructure design and even involves the utilization of expensive raw materials or toxic agents, which conflicts with the intrinsic merits of the RT Na-S battery. Developing facile and favorable strategies to effectively trap NaPSs is one of the most urgent aspects.

In the current RT Na-S battery, the most widely used current collector (CC) is aluminum (Al) foil because of its lightweight and electrochemical/chemical inertia towards NaPSs. The inertia property of Al-CC means that it cannot build a robust interface between the Al-CC and the electrode. Moreover, the poor adhesion of sulfur cathodes on the planar Al-CC usually leads to inferior cycling performance, especially at high sulfur loading[19,20]. However, there are few works focusing on the engineering of the electrode/CC interface of the sulfur cathode despite its critical importance. In comparison, the Cu-CC is rarely applied in the Na-S battery system due to its spontaneous reaction with NaPSs[21,22], which will corrode the Cu-CC. However, if regulated in a controlled manner, the Cu-CC is capable of affording strong chemical interaction with NaPSs because of its significant sulfiphilicity[22]. Moreover, the chemical interaction between Cu and NaPSs may create a robust Cu/electrode interface and stabilize the electrode structure. Further, the generated interface can help to capture the NaPSs and suppress the shuttle effect due to its polar characteristics[23,24]. Recently, a high-rate and long-life RT Na-S battery was reported by using an amorphous silica host and Cu-CC in an ether electrolyte[25]. The authors attributed the excellent performances to the strong adsorption of the silica host. However, the critical roles of sulfiphilic Cu in the ether-based electrolyte may be ignored. Therefore, it is highly desirable to unveil the reaction mechanisms of the Na-S battery with Cu-CC and clarify the role of the electrode/CC interface in the Na-S batteries.

Herein, by using the Cu foil as the CC in ether electrolyte, we systematically study the Na-S chemistry in terms of electrochemical performance, reaction mechanisms, and electrode/Cu-CC interface evolution. We first studied the Na-S batteries with carbon nanotube (CNT)/S cathodes and Cu-CC. We found the CNT/S cathode could achieve an excellent rate performance (447.3 mAh g^{-1} at 8.0 A g^{-1}) and long lifespan (98.3% capacity retention after 1,300 cycles) in ether electrolytes due to the strong chemical interaction between Cu-CC and NaPSs. However, this chemical interaction induces serious Cu corrosion (~26.3%). To suppress the Cu corrosion and take advantage of the Cu-CC/NaPS interaction, we use the Cu@CNT/S cathode to re-evaluate the Cu corrosion situation and electrochemical mechanism. The results reveal that the Cu@CNT/S cathode is gradually converted to NaPS@Cu_7S_4 nanoparticles (~11 nm), leading to robust sulfur immobilization and enhanced Na^+ reaction kinetics. Moreover, similar to the CNT/S cathode, a part of NaPSs chemically interacts with Cu-CC, realizing an intimate Cu/electrode interface and ultra-low interfacial resistance (< 4 Ω). This kind of battery can be deemed as a quasi-Na-S battery. Notably, the chemical interaction between NaPSs and Cu-CC induces a much-limited Cu-CC corrosion degree (~3.8%) based on a Cu-CC with a thickness of 8 μm. This low Cu-CC corrosion degree is quite acceptable in practical applications[26]. More importantly, the quasi-Na-S battery can achieve excellent electrochemical performance in terms of cycle life (nearly no capacity decay over 1,190 cycles) and rate capability (396.9 mAh g^{-1} at 10 A g^{-1}).

RESULTS AND DISCUSSION

To reveal the critical role of the CC and electrolyte in Na-S batteries, we compared the cycling performance with different CCs (Cu, Al) and electrolytes (1, 2-dimethoxyethane (DME), ethylene carbonate/diethyl carbonate (EC/DEC)) [Figure 1]. The CNT/S composite with a sulfur content of 50 wt% was used as the cathode. Firstly, we evaluated the performance of DME electrolytes with Cu-CC and Al-CC. As shown in Figure 1A, the Na-S cell with Cu-CC (DME-Cu) delivers high initial discharge/charge capacities of 572.0/508.8 mAh g^{-1} at 0.5 A g^{-1}, showing a high initial Coulombic efficiency (ICE) of 88.9%. Moreover, the DME-Cu system exhibits a high capacity of 491.5 mAh g^{-1} after 1,300 cycles [Figure 1B], holding a high-capacity retention of 98.3% (*vs.* 2nd cycle). In contrast, the Na-S cell with Al-CC (DME-Al) delivers much lower initial discharge/charge capacities of 151.7/343.1 mAh g^{-1} at 0.5 A g^{-1}, which rapidly drops to 42.9 mAh g^{-1} after 300 cycles. These results indicate that the Cu-CC plays a critical role in improving the specific capacity and cyclic stability of the CNT/S cathode[27]. Moreover, the DME-Cu system presents a much better rate capability than the DME-Al system [Figure 1C]. At a high current density of 8.0 A g^{-1}, the DME-Cu system delivers a high capacity of 447.3 mAh g^{-1}. Considering only commercial CNT was used to host the sulfur cathode, the rate performance is highly competitive in the current Na-S battery systems. The enhanced performance of DME-Cu systems should be ascribed to the super sulfiphilicity of Cu that could efficiently trap the NaPSs[21]. As demonstrated in Supplementary Figure 1 and Supplementary Figure 2, when soaking the Cu foil in Na_2S_4 solution, an obvious Cu reaction is observed, indicating the rapid chemical reaction between Na_2S_4 and Cu. In contrast, the Al foil shows no change within the Na_2S_4 solution. Since the Al foil cannot chemically interact with the NaPSs, the generated NaPSs will shuttle to the anode side through the separator [Supplementary Figure 3], leading to rapid capacity fading. Notably, due to the mass transfer limitation, the generated NaPSs on top of the electrode (away from the Cu/electrode interface) cannot be timely trapped by the Cu-CC, which inevitably results in partial NaPSs shuttling. Thus, the DME-Cu system shows an obvious capacity drop in the initial cycles [Figure 1B]. However, different from the DME-Al system, the shuttled NaPSs could be gradually activated in the subsequent cycles due to the chemical interaction between Cu-CC and NaPSs since this activation process was not observed in the DME-Al system.

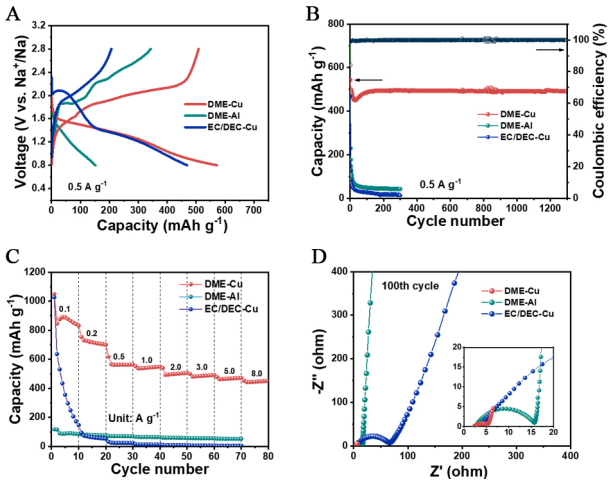

Figure 1. Electrochemical performance of CNT/S electrodes with different electrolytes and current collectors. (A) Initial charge/discharge profiles; (B) Cycling performance at 0.5 A g^{-1}; (C) Rate capability at various current densities; (D) Nyquist plots after 100 cycles.

Further, we compared the cycling performance of Na-S batteries in ether and carbonate electrolytes using the Cu foil as the CC. As shown in Figure 1A, the Na-S cell in EC/DEC electrolyte (EC/DEC-Cu) delivers initial discharge/charge capacities of 469.0/260.6 mAh g^{-1} at 0.5 A g^{-1}, much lower than those in DME electrolyte. Moreover, the EC/DEC-Cu system exhibits a much worse cycling performance, with a capacity of only 13.6 mAh g^{-1} after 300 cycles [Figure 1B]. The rate performance shows a near-zero capacity at a low current density of 1 A g^{-1} [Figure 1C], indicating highly sluggish reaction kinetics. The inferior performance of EC/DEC-Cu electrolytes may be ascribed to the following reasons[28]: (1) The Na-S battery in carbonate electrolytes is based on quasi-solid conversion processes, which undergo highly sluggish conversion reactions; (2) The parasitic nucleophilic addition/substitution reactions between NaPSs and carbonate solvents lead to irreversible active material loss. The sluggish conversion reactions and parasitic reactions inevitably result in low sulfur utilization, short cycle life, and poor rate performance.

Figure 1D depicts the electrochemical impedance spectra (EIS) of DME-Cu, DME-Al, and EC/DEC-Cu systems after 100 cycles. All the impedance spectra exhibit one semicircle in the high-frequency regions, representing the charge transfer resistance (R_{ct})[29]. Compared to an EC/DEC-Cu system, the DME-Cu system shows much smaller R_{ct} (~3 Ω). The low R_{ct} should be due to the better wettability of DME solvents than the EC/DEC solvent[30]. Moreover, the better solubility of NaPSs in DME favors solid–liquid sulfur conversion and electrochemical redox on the electrode/electrolyte interface[31,32]. With the same DME electrolyte, the DME-Cu system presents smaller R_{ct} than the DME-Al system, suggesting the chemical interaction between NaPSs and Cu foil can significantly reduce the R_{ct}, possibly through forming conductive materials and creating an intimate connection between Cu and electrode. This inference will be confirmed in the later section. The ultralow R_{ct} value indicates the greatly improved redox reaction kinetics in DME-Cu systems, which results in excellent rate performance. Moreover, over the cycling performance, the interfacial resistance in DME-Cu systems always remains at low values (< 4 Ω), indicating a stable and favorable reaction process [Supplementary Figure 4].

To unveil the excellent performance of Na-S batteries with ether electrolytes and Cu-CC, we studied the structure evolution of the CNT/S electrode. The pristine CNT/S powder (the sulfur loading is 56%) consists of typical monoclinic S_8 without other impurities [Supplementary Figure 5][33]. After being coated on the Cu foil and vacuum dried at 60 ℃, the X-ray diffraction (XRD) pattern of the CNT/S electrode shows obvious

peaks from hexagonal CuS (JCPDS No. 03-65-3556), indicating that the S will react with Cu foil during the electrode preparation [Figure 2A and Supplementary Figure 6A]. The Cu LM2 auger electron spectrum (AES) of CNT/S electrodes shows an obvious peak at 917.9 eV, corresponding to the Cu^+ in CuS [Figure 2B][34]. As for the S 2p XPS spectra [Figure 2C], the CNT/S electrode maintains the major peaks from S^0. In addition, two pairs of peaks at 161.8 eV ($2p_{3/2}$) and 162.6 eV ($2p_{3/2}$) belong to S^{2-} and S_2^- of CuS, respectively[35,36]. The cross-section elemental mapping images of the CNT/S electrode [Supplementary Figure 6B] reveal that the Cu and S signals mainly appear at the bottom of the electrode, indicating that the sulfur is mainly located at the Cu-CC/electrode interface due to the chemical reaction with Cu-CC. Scanning electron microscopy (SEM) and transmission electron microscopy (TEM) images reveal that the CuS has an average size of around 50 nm [Supplementary Figure 6C and Supplementary Figure 7].

To explore the structural evolution of the CuS-S_8/CNT upon cycling, a series of ex-situ measurements have been conducted. Supplementary Figure 8 reveals that the discharge-charge profiles gradually evolve upon the cycling and become steady until 80 cycles, indicating that the electrode material undergoes irreversible phase transformation. Figure 2A shows the XRD patterns of the CuS-S_8/CNT at different cycles. The pristine electrode consists of S_8 and CuS. After the 1st cycle, the XRD pattern shows a set of diffraction peaks at 28.6°, 29.8°, and 52.4°, possibly belonging to the $Na_xCu_yS_z$[37-39]. In addition, the peaks at 39.2° and 46° are assigned to cubic Na_2S (JCPDS No. 00-23-0441), and the peaks at 46.6° and 48.8° are indexed to hexagonal Cu_2S (JCPDS No. 01-89-2670). As for the S_8 component in the electrode, it will firstly react with Na^+ to form NaPSs ($NaS_{x'}$) and then dissolve into the electrolyte due to their high solubility in DME electrolytes[27]. Subsequently, $NaS_{x'}$ will spontaneously react with Cu-CC to form Cu_2S due to the super sulfiphilicity of Cu-CC [Supplementary Figure 2A][21]. The whole reaction in the first cycle can be described as:

$$\mathrm{CuS} + Na^+ + e^- \rightarrow Na_xCu_yS_z + Na_2S \quad (1)$$

$$S_8 + Na^+ + e^- \rightarrow NaS_{x'} \text{ (Electrochemical reaction)} \quad (2)$$

$$NaS_{x'} + Cu - e^- \rightarrow Cu_2S + Na^+ \text{ (Chemical reaction)} \quad (3)$$

After ten cycles, the signal of Cu_2S becomes more obvious; meanwhile, the peaks of Na_2S become weak, and those of $Na_xCu_yS_z$ completely disappear [Figure 2A]. The Na_2S consumption upon the cycling indicates that the Cu-CC is capable of activating the Na_2S decomposition. The reactions can be described as:

$$Na_2S - e^- \rightarrow NaS_{x'} + Na^+ \text{ (Electrochemical reaction)} \quad (4)$$

$$NaS_{x'} + Cu - e^- \rightarrow Cu_2S + Na^+ \text{ (Chemical reaction)} \quad (5)$$

$$Na_2S + Cu - 2e^- \rightarrow Cu_2S + Na^+ \quad (6)$$

After 80 cycles, the Na_2S completely disappears, and only peaks from Cu_2S can be observed. Even after 100 cycles, the XRD pattern still shows the peaks of Cu_2S [Supplementary Figure 9], indicating that Cu_2S is a highly reversible phase in the subsequent cycles.

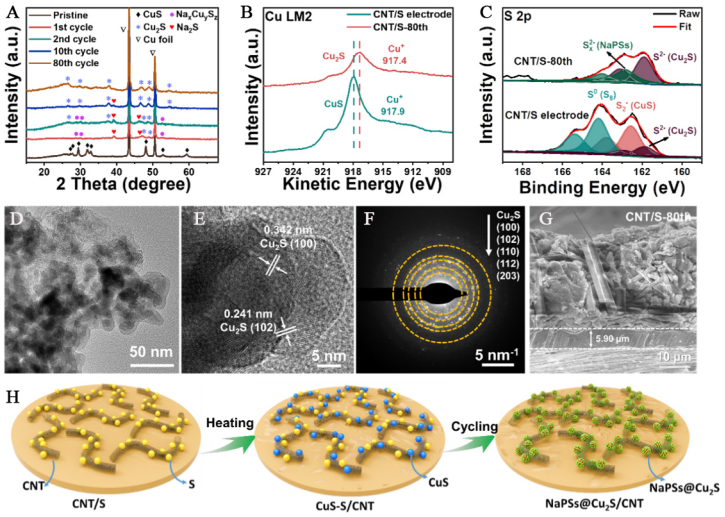

Figure 2. CNT/S electrode evolution. (A) XRD patterns at pristine and different cycles of CNT/S electrode; (B) Cu LM2 auger electron spectroscopy and (C) S 2p XPS spectra of pristine and 80th cycle electrode; (D) TEM image; (E) HRTEM image; (F) SAED pattern; (G) Cross-section SEM of the CNT/S electrode after 80 cycles; and (H) Schematic diagram of CNT/S electrode evolution

To further study the detailed structure of the CNT/S electrode after 80 cycles, we performed the X-ray photoelectron spectroscopy (XPS) and AES. The Cu LM2 auger transition is 917.4 eV for the CNT/S-80th electrode, consistent with the value for Cu_2S [Figure 2B][36]. The S 2p XPS spectra after 80 cycles show a pair of doublet peaks at 161.8 eV (S $2p_{3/2}$) and 163.0 eV (S $2p_{1/2}$), corresponding to the Cu_2S [Figure 2C]. In addition, other doublet peaks at 162.8 eV (S $2p_{3/2}$) and 164.0 eV (S $2p_{1/2}$) belong to the polysulfides[40]. The remaining polysulfides in the CNT/S-80th electrode may originate from the adsorbed polysulfides on the polar Cu_2S surface, which can serve as active materials in the subsequent cycles. Hence, the sulfur was successfully captured by both the Cu and Cu_2S, forming the NaPS@Cu_2S/CNT composite. Compared with the electron-insulating S, the formed Cu_2S shows much higher electron conductivity, which significantly improves the charge transfer kinetics[41]. SEM and TEM images reveal that the as-formed Cu_2S nanoparticles show an average size of around 20 nm [Supplementary Figure 10 and Figure 2D]. A high-resolution transmission electron microscope (HRTEM) image presents clear lattice fringes with interplanar spacing of 0.342 nm, corresponding to the (100) plane of Cu_2S [Figure 2E]. The selected area electron diffraction (SAED) pattern focused on nanoparticles displays several diffraction rings that can be accurately indexed to the Cu_2S [Figure 2F]. The STEM-EDX elemental mapping images show the uniform distribution of Cu, S, and Na elements through the whole electrode material [Supplementary Figure 11], suggesting the uniform combination of Cu_2S and NaPSs. The special structure not only ensures fast and continuous electron transfer but also enables superior sodium storage kinetics due to the shortened Na^+ diffusion length in Cu_2S nanocrystals.

However, it should be noted that the participation of Cu-CC in the chemical reaction will cause the Cu corrosion. As shown in the cross-section SEM images [Supplementary Figure 12], after being coated with the CNT/S cathode (sulfur loading: 1 mg cm^{-2}), the Cu thickness reduces to 6.73 μm (*vs.* the pristine Cu-CC: 8.0 μm). After 80 cycles (steady state), the thickness of Cu foil further reduces to 5.90 μm, showing a Cu corrosion ratio of 26.3% [Figure 2G]. Despite corrosion, the Cu-CC still shows a close connection with the electrode. Moreover, the Cu corrosion can enhance the contact area and roughness of the Cu-CC, which could stabilize the electrode/Cu-CC interface and reduce the contact resistance[26,42]. However, the severe Cu-CC corrosion will induce potential safety hazards. When the sulfur loading is increased to 3.5 mg cm^{-2}, it seriously damages the Cu-CC, leading to the Na-S battery failure [Supplementary Figure 13]. As a result, the

overall structure evolution of the CNT/S electrode with ether electrolytes and Cu-CC is illustrated in Figure 2H.

To ensure the successful operation of Na-S batteries, the Cu corrosion degree should be well restricted. A viable strategy is to trap the dissolved NaPSs and restrict the chemical reaction between Cu-CC and NaPSs. Inspired by the reaction mechanisms mentioned above, Cu@CNT with a CNT content of 36.5 wt% was proposed as the new host material for Na-S batteries [Supplementary Figure 14]. The schematic illustration of the preparation is shown in Supplementary Figure 15. The incorporation of Cu@CNT in the cathode mimics the Cu foil to chemically trap the NaPSs and form active copper sulfide. Moreover, the formed copper sulfide can serve as anchoring sites to capture NaPSs. As shown in Supplementary Figure 16, when the sulfur is loaded into the Cu@CNT, the composite becomes the CuS-S_8@CNT (Sulfur loading around 1 mg cm^{-2}). After 80 cycles at 0.5 A g^{-1}, the XRD pattern of the electrode shows obvious peaks of Cu_7S_4 (JCPDS No. 023-0958, Figure 3A), which is different from the CNT/S-80th electrode (formation of Cu_2S) due to the different reaction routes. SEM and TEM images reveal that the Cu_7S_4 nanoparticles with an average size of 11 nm are embedded in the CNT network [Supplementary Figure 17 and Figure 3B]. A HRTEM image shows clear lattice fringes with an interplanar distance of 0.194 nm, corresponding to the (0160) plane of Cu_7S_4 [Figure 3C]. SAED pattern with several diffraction rings further confirms the formation of monoclinic Cu_7S_4 (JCPDS No. 023-0958) after 80 cycles [Figure 3D]. In order to further prove the form of Cu_7S_4 in the Cu@CNT/S-80th electrode, we conduct the AES and XPS spectra of Cu in the Cu@CNT/S electrode [Supplementary Figure 18]. The AES of Cu LM2 and XPS of Cu 2p show obvious peaks at 917.2 eV, 932.8 eV, and 952.6 eV, corresponding to the Cu_7S_4[43]. S *2p* XPS spectra of the Cu@CNT/S-80th electrode exhibit two pairs of peaks [Figure 3E]: the doublet peaks at 161.5 and 162.7 eV correspond to the S $2p_{3/2}$ and S $2p_{1/2}$ of Cu_7S_4, respectively[43,44], and the peaks at 162.2 and 163.4 eV belong to polysulfide species (S_x^{2-}). Similar to the CNT/S electrode, the existence of S_x^{2-} in the Cu@CNT/S-80th electrode suggests the formation of NaPSs@Cu_7S_4/CNT composite after 80 cycles. The presence of the NaPSs in the steady state also proves that the newly formed Cu_7S_4 can adsorb the NaPSs and prevent their diffusion to the Cu-CC.

Then, we detect the cross section of the electrode to assess the Cu-CC/electrode interface. As shown in Figure 3F, the Cu-CC of the pristine Cu@CNT/S electrode shows a thickness of 7.96 μm, corresponding to a low corrosion ratio of 0.5%. After 80 cycles, the Cu thickness reduces to 7.70 μm [Figure 3G], showing a low Cu corrosion ratio of only 3.8%. This value is much smaller than that of the CNT/S electrode, suggesting that the incorporation of Cu@CNT composites can significantly suppress the Cu corrosion. Notably, this low Cu corrosion ratio (3.8%) is quite acceptable in practical applications because the thickness of Cu foil used in commercial batteries is usually larger than 6 μm[26]. The greatly depressed Cu corrosion is due to the reduced NaPS outflow from the cathode. As shown in the cross-section SEM-EDS elemental mapping images [Figure 3G], the sulfur signal is uniformly distributed over the electrode without obvious enrichment at the electrode/Cu-CC interface, which is quite different from the CNT/S electrode. This is because the presence of Cu in Cu@CNT/S affects the reaction routes and products between NaPSs and Cu-CC. In the CNT/S system, most of the S participates in the reaction with Cu-CC within the cathode/CC interface; thus, the Cu and S signals mainly appear at the bottom of the electrode. Moreover, the Cu-CC is seriously corroded. However, in the case of a Cu@CNT/S system, most of the S reacts with Cu in the Cu@CNT/S, maintaining the S signal mainly in the electrode. Only a small part of NaPSs diffuse to the Cu-CC and react with Cu-CC to form a weak Cu_7S_4 interface. The reduced NaPS diffusion from the electrode to the Cu-CC surface greatly depresses the Cu-CC corrosion. Moreover, the electrode shows intimate contact [Figure 3G] with Cu-CC due to the chemical interaction between the NaPSs and Cu-CC, which could significantly enhance the electrode stability and reduce the contact resistance. To further investigate the interface, we measured the morphology of the Cu-CC surface. The pristine Cu-CC shows irregular protuberances with

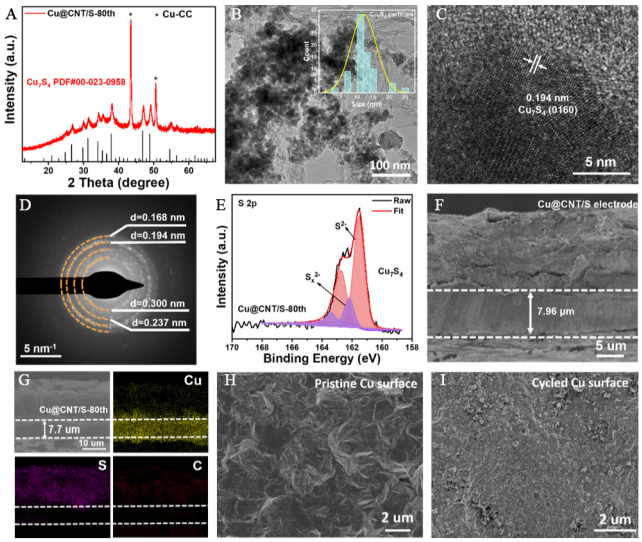

Figure 3. Structural characterization of the Cu@CNT/S electrode after 80 cycles. (A) XRD pattern; (B and C) TEM images, inset in (B) is the size distribution diagram, (D) SAED pattern, and (E) S *2p* XPS spectrum of Cu@CNT/S electrode after 80 cycles. Cross-section SEM image of the pristine Cu@CNT/S electrode (F) and cycled Cu@CNT/S electrode after 80 cycles (G). SEM images of the pristine Cu-CC surface (H) and cycled Cu-CC surface after 80 cycles (I).

sizes around 2~6 μm [Figure 3H and Supplementary Figure 19A]. After 80 cycles, the Cu-CC shows a rough surface consisting of closely connected nanoparticles [Figure 3I and Supplementary Figure 19B], corresponding to the copper sulfide nanoparticles. The nanoparticles tightly adhere to the Cu-CC surface and serve as the "linkers" to stabilize the electrode/Cu-CC interface, which significantly improves the electrode stability and, thus, the cycling performance. Remarkably, when increasing the sulfur loading to 3.5 mg cm^{-2}, the pristine Cu@CNT/S and cycled electrode show low Cu corrosion of 3.75% and 5.88%, respectively [Supplementary Figure 20], demonstrating the Cu@CNT/S electrode is applicable for high sulfur loading applications.

Then, we evaluated the sodium storage performance of Cu@CNT/S within the voltage window of 0.8~2.8 V. As shown in Figure 4A, the Cu@CNT/S delivers high initial discharge/charge capacities of 681/565.8 mAh g^{-1} at 0.5 A g^{-1}, showing a high ICE of 83%. Moreover, the average discharge plateau is around 1.2~1.75 V, which is comparable to those in the Na-S battery with carbonate electrolytes[8,16,45,46]. After 430 cycles, the capacity of Cu@CNT/S remains at 532.6 mAh g^{-1}, corresponding to a capacity retention of 95.2% (*vs.* 2nd cycle) [Supplementary Figure 21]. Moreover, the Cu@CNT/S electrode demonstrates an excellent rate capability [Figure 4B]. Even at a high current density of 10 A g^{-1}, the Cu@CNT/S electrode delivers a high capacity of 396.9 mAh g^{-1}. The excellent rate capability can be ascribed to the formation of NaPS@Cu_7S_4 with enhanced reaction kinetics and the intimate Cu/electrode interface that enables fast charge transfer. Then, we measured the long-term cycling performance of the Cu@CNT/S electrode at 3 A g^{-1} [Figure 4C]. The cycling performance can be divided into three stages. Stage I shows a fast capacity drop, which should be ascribed to the local NaPSs shuttling. In stage II, the capacity gradually increases until the 200th cycle, suggesting the dissolved NaPSs are gradually trapped by both the Cu@CNT and Cu-CC and converted to NaPS@copper sulfide. This can be further confirmed by the cycling performance of CNT/S [Figure 1B] and Cu@CNT/S electrodes [Supplementary Figure 22A] with Al-CC, where the former shows no capacity increases while the latter delivers weak capacity increase from the 20th to 60th cycle. In stage III, a high capacity of 485.9 mAh g^{-1} is achieved after 1,190 cycles [Figure 4C], showing a high-capacity retention of ~100%. The ultra-stable cycling is attributed to the robust Cu-CC/electrode interface created by the NaPSs-

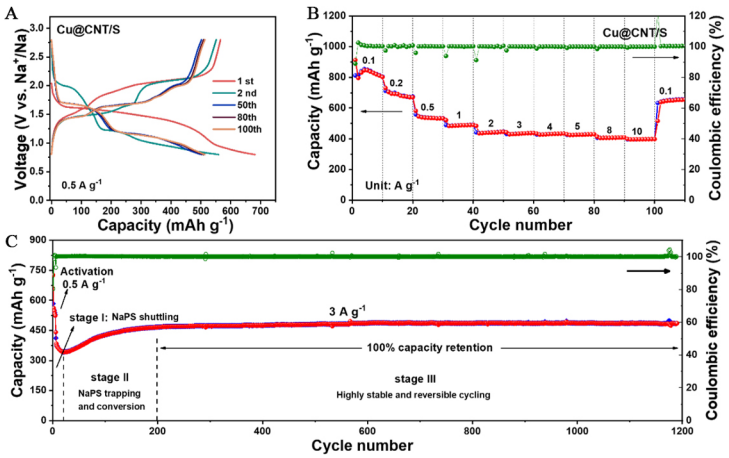

Figure 4. Electrochemical performance of Cu@CNT/S electrodes. (A) Charge-discharge profiles at different cycles; (B) Rate capability at various current densities; (C) Long-term cycling performance at 3 A g^{-1}.

Cu chemical interaction. In contrast, the Cu@CNT/S electrode with Al-CC cannot establish the NaPSs-Al chemical interaction, thus leading to a capacity drop starting from the 60th cycle [Supplementary Figure 22A]. Moreover, the Cu@CNT/S with Al-CC delivers poor rate capability [Supplementary Figure 22B], demonstrating that the slight Cu elicitation (3.8%) plays a critical role in improving the reaction kinetics. The EIS spectra of the Cu@CNT/S electrodes with Cu-CC and Al-CC are compared in Supplementary Figure 23. After 50 cycles, the Cu@CNT/S electrode with Cu-CC delivers an ultra-small resistance of less than 6 Ω, confirming the construction of a favorable electrode/Cu-CC interface is beneficial for the kinetics enhancement. Overall, the Cu@CNT/S electrode with Cu-CC exhibits excellent cycling/rate performances, which are highly competitive in comparison to the current Na-S battery systems [Supplementary Table 1].

To confirm the excellent reaction kinetics, we quantified the pseudocapacitive contributions in the Cu@CNT/S electrode based on the cyclic voltammetry (CV) curves at various scan rates [Supplementary Figure 24]. Through calculation, the Cu@CNT/S electrode exhibits a large pseudocapacitive contribution of 92% at 0.2 mV s^{-1} and 97% at 1 mV s^{-1}, suggesting its outstanding pseudocapacitive behavior[47,48]. It provides unambiguous evidence that the high ratio of the pseudocapacitive contribution enables fast Na^+ transport; therefore, the Cu@CNT/S electrode delivers excellent rate capability.

Based on the above analysis, the function mechanisms of the RT Na-S battery with different sulfur hosts and CCs (in ether electrolyte) are illustrated in Figure 5. When using the bare CNT host and Al-CC, the NaPSs are prone to dissolve into the ether electrolyte and shuttle to the anode side, causing rapid capacity decay [Figure 5A]. When the CNT host and Cu-CC were used in the Na-S battery [Figure 5B], the NaPSs were dissolved into an ether electrolyte and then gradually captured by the Cu-CC, resulting in a limited NaPSs shuttle effect and a more robust CC/electrode interface. Thus, excellent rate capability and ultralong cycle life can be achieved. However, this battery configuration causes serious corrosion of Cu-CC. With the Cu@CNT host and Al-CC [Figure 5C], the shuttle effect of NaPSs can be partly suppressed by the Cu@CNT host, and CC corrosion can be avoided, but the electrochemical performance is dissatisfactory due to the weak CC/electrode interface and still-existing NaPSs shuttle effect. Remarkably, with the Cu@CNT host and Cu-CC [Figure 5D], the NaPSs experience two main reaction routes in Na-S batteries. The major NaPSs are trapped by Cu@CNT to form NaPSs@Cu_2S_4/CNT, which could enhance the electronic conductivity and reduce the Cu foil corrosion; the remaining NaPSs interact with Cu foil to form the intimate Cu/electrode

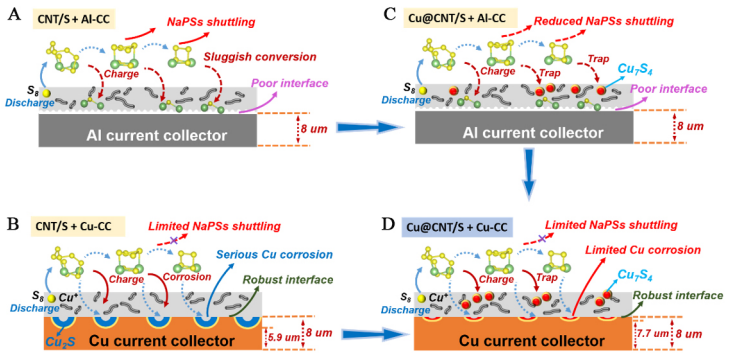

Figure 5. Schematic illustration of the function mechanism of the Na-S batteries with different sulfur hosts and current collectors in ether electrolytes. (A) CNT/S with Al-CC and (B) Cu-CC in DME electrolytes; (C) Cu@CNT/S with Al-CC and (D) Cu-CC in DME electrolytes.

interface, which significantly enhances the charge transfer kinetics and electrode stability. Because of the phase transformation, the type-iv battery system can be deemed as a quasi-Na-S battery. The electrode transformation and reconstruction show several advantages. Firstly, the sulfiphilic Cu and obtained Cu_7S_4 can chemically trap the sulfur species and suppress the polysulfide shuttling effect, resulting in stable cycling performance. Secondly, the controllable reaction between Cu-CC and NaPSs builds a robust electrode/CC interface favorable for electrode stabilization. Thirdly, compared with the electrically insulated S_8, the obtained Cu_7S_4 shows much higher electron conductivity, which significantly improves the charge transfer kinetics. Lastly, the formed Cu_7S_4 nanoparticles (~11 nm) are uniformly distributed in the CNT network, which ensures superior sodium storage kinetics. Thus, this quasi-Na-S battery realizes high sodium storage performance and reduced Cu foil elicitation (~3.8%). The high performance and lost cost of the RT Na-S battery with Cu@CNT host and Cu-CC is highly competitive for the cost-sensitive grid-scale applications.

CONCLUSION

In summary, we have demonstrated that the CNT/S cathode, without complicated immobilization, can realize high sodium storage performance in a quasi-Na-S battery with the DME solvent and Cu-CC. Ex situ measurements reveal that the CNT/S was gradually converted to NaPSs@Cu_2S/CNT composites, enabling highly favorable Na^+ reaction kinetics and simultaneously building a robust electrode/Cu-CC interface. However, the electrode reconstruction is accompanied by serious Cu foil corrosion, which is detrimental to practical applications. Alternatively, a Cu@CNT host material was adopted to mimic the Cu-CC and trap the sulfur cathode, which demonstrates the greatly depressed Cu foil corrosion (reduced to 3.8%) and, meanwhile, fully takes advantage of the Cu foil elicitation with enhanced Cu/electrode interface and Na^+ reaction kinetics. Due to the synergetic effect of effective polysulfide capture and robust Cu/electrode formation, this type of quasi-Na-S battery delivers an excellent rate capability (396.9 mAh g^{-1} at 10 A g^{-1}) and ultra-stable cycling performance (nearly no capacity decay over 1,190 cycles). This work would encourage the community to apply low-cost sulfur cathode and Cu-CC in Na-S batteries in a controlled manner.

Experimental section

Preparation of Cu@CNT: 100 mg of CNT was dispersed into 40 mL of deionized water with ultrasonication for 30 mins. Then, 400 mg of $Cu(CH_3COO)_2 \cdot H_2O$ was dissolved in the above solution with ultrasonication for 2 h. Next, the solution was transferred to an evaporating dish and heated at 100 ℃ for 12 h to get the black powder. Finally, the Cu@CNT powder was obtained by annealing the black powder at 350 ℃ for 1 h in air and then at 500 °C for 2 h under an H_2/Ar atmosphere (v:v = 8%: 92%).

Preparation of CNT/S and Cu@CNT/S: To prepare the CNT/S, the sublimed sulfur was mixed with the CNT with a sulfur loading of 56%. Then, the black powder is sealed in a glass tube under vacuum, followed by heating the glass tube at 155 °C for 15 h. To prepare the Cu@CNT/S, the Cu@CNT was loaded with sulfur using the same procedure.

Material characterization: The crystalline structures were analyzed by an XRD diffractometer (40 kV, 40 mA, Bruker D8 Advance) with Cu Kα radiation. The XPS and AES spectra were recorded by using the Thermo Fisher EscalableXi+ equipment. The morphological and structural information was obtained by SEM (Hitachi SU8010) and TEM (Thermo Fisher TALOS F200X, acceleration voltage: 200 kV). TG curve was acquired by TG209 F3 from 40 °C to 700 °C at a constant heating rate of 10 °C min^{-1} in air.

Electrochemical measurement: To obtain the electrode, active materials (CNT/S or Cu@CNT/S), Sodium carboxymethylcellulose (CMC), and Ketjen Black were mixed with a mass ratio of 8: 1: 1 and stirred in distilled water for 30 mins to generate the slurry. Next, the slurry was coated on Cu (or Al) foil and dried in a vacuum oven at 60 °C for 12 h. The thicknesses of the Cu and Al foils are 8 um and 20 um, respectively (Suzhou Sinero Technology Co., Ltd.), with one-side smooth. The electrode was cut into round pieces with a diameter of 12 mm. The average sulfur loading is about 1.0 mg cm^{-2}. For high-loading measurement, the electrode with sulfur loading of 3.5 mg cm^{-2} was also prepared. Then, the electrode was assembled based on the CR2032 coin cells in an Ar-filled glove box. 1 M $NaPF_6$ in DME (or 1 M $NaPF_6$ in EC/DEC) served as the electrolyte. The galvanostatic charge-discharge performances are tested within a voltage window of 0.8-2.8 V by a Neware battery test system. The capacities of all the cells are calculated based on the mass of sulfur. CV and EIS (100 k to 10 mHz) measurements were tested on an electrochemical workstation (IVIUMnSTAT).

DECLARATIONS

Acknowledgments

This work was supported by the National Natural Science Foundation of China (Grant Number: 22109183). Additionally, the project was aided by the State Key Laboratory of Advanced Technology for Materials Synthesis and Processing (Wuhan University of Technology, 2023-KF-17) and "the Fundamental Research Funds for the Central Universities" at South-Central MinZu University (Grant Number: CZZ23002).

Authors' contributions

Contributed equally to the paper and carried out most of the experiments and tests: Song H, Li T
Performed cross-section SEM and TEM tests: He T, Chen G
Measured the XRD: Kong D
Contributed to discussions and interpretation of results: Yan D
Conceived the experiments and participated in writing the manuscript: Yang HY, Huang S
All authors have approved the final manuscript: Song H, Li T, He T, Chen G, Deng C, Kong D, Yan D, Yang HY, Huang S

Availability of data and materials

The data supporting this article have been included as part of the Supplementary Materials.

Financial support and sponsorship

This work was supported by the National Natural Science Foundation of China (Grant Number: 22109183). Additionally, the project was aided by the State Key Laboratory of Advanced Technology for Materials Synthesis and Processing (Wuhan University of Technology, 2023-KF-17) and "the Fundamental Research Funds for the Central Universities" at South-Central MinZu University (Grant Number: CZZ23002).

Conflicts of interest

All authors declared that there are no conflicts of interest.

Ethical approval and consent to participate

Not applicable.

Consent for publication

Not applicable.

Copyright

© The Author(s) 2023.

REFERENCES

1. Yan Z, Liang Y, Xiao J, et al. A high-kinetics sulfur cathode with a highly efficient mechanism for superior room-temperature Na-S batteries. *Adv Mater* 2020;32:e1906700. DOI
2. Li Z, Wang C, Ling F, et al. Room-temperature sodium-sulfur batteries: rules for catalyst selection and electrode design. *Adv Mater* 2022;34:e2204214. DOI
3. Hao H, Hutter T, Boyce BL, Watt J, Liu P, Mitlin D. Review of multifunctional separators: stabilizing the cathode and the anode for alkali (Li, Na, and K) metal-sulfur and selenium batteries. *Chem Rev* 2022;122:8053-125. DOI
4. Wang L, Wang T, Peng L, et al. The promises, challenges and pathways to room-temperature sodium-sulfur batteries. *Natl Sci Rev* 2022;9:nwab050. DOI
5. Zhou X, Yu Z, Yao Y, et al. A high-efficiency Mo_2C electrocatalyst promoting the polysulfide redox kinetics for Na-S batteries. *Adv Mater* 2022;34:2200479. DOI
6. Xing C, Chen H, Qian S, et al. Regulating liquid and solid-state electrolytes for solid-phase conversion in Li-S batteries. *Chem* 2022;8:1201-30. DOI
7. Li S, Zhang W, Zeng Z, Cheng S, Xie J. Selenium or tellurium as eutectic accelerators for high-performance lithium/sodium-sulfur batteries. *Electrochem Energ Rev* 2020;3:613-42. DOI
8. Xiao F, Yang X, Wang H, et al. Covalent encapsulation of sulfur in a MOF-derived S, N-doped porous carbon host realized via the vapor-infiltration method results in enhanced sodium-sulfur battery performance. *Adv Energy Mater* 2020;10:2000931. DOI
9. Tzadikov J, Levy NR, Abisdris L, et al. Bottom-up synthesis of advanced carbonaceous anode materials containing sulfur for Na-ion batteries. *Adv Funct Materials* 2020;30:2000592. DOI
10. Yang G, Zhou Z, Liu X, et al. Bowl-shaped hollow carbon wrapped in graphene grown in situ by chemical vapor deposition as an advanced anode material for sodium-ion batteries. *J Colloid Interface Sci* 2023;637:283-90. DOI
11. Liu X, Si Y, Li K, et al. Exploring sodium storage mechanism of topological insulator Bi2Te3 nanosheets encapsulated in conductive polymer. *Energy Storage Mater* 2021;41:255-63. DOI
12. Yan Z, Xiao J, Lai W, et al. Nickel sulfide nanocrystals on nitrogen-doped porous carbon nanotubes with high-efficiency electrocatalysis for room-temperature sodium-sulfur batteries. *Nat Commun* 2019;10:4793. DOI PubMed PMC
13. Aslam MK, Seymour ID, Katyal N, et al. Metal chalcogenide hollow polar bipyramid prisms as efficient sulfur hosts for Na-S batteries. *Nat Commun* 2020;11:5242. DOI PubMed PMC
14. Yang G, Zhou Z, Liu X, et al. Bowl-shaped carbon loaded Co9S8 nanoparticles connected by carbon nanotubes with excellent rate performance for sodium-ion batteries. *Electrochimica Acta* 2023;441:141804. DOI
15. Li Z, Yang Y, Wen B, et al. Recovered cobalt-nickel sulfide from spent lithium-ion batteries as an advanced anode material toward sodium-ion batteries. *J Alloy Compd* 2023;956:170328. DOI
16. Zhang S, Yao Y, Jiao X, et al. Mo_2 N-W_2N heterostructures embedded in spherical carbon superstructure as highly efficient polysulfide electrocatalysts for stable room-temperature Na-S Batteries. *Adv Mater* 2021;33:e2103846. DOI
17. Zhou D, Tang X, Guo X, et al. Polyolefin-based janus separator for rechargeable sodium batteries. *Angew Chem Int Ed Engl* 2020;59:16725-34. DOI
18. Huang XL, Wang YX, Chou SL, Dou SX, Wang ZM. Materials engineering for adsorption and catalysis in room-temperature Na-S batteries. *Energy Environ Sci* 2021;14:3757-95. DOI
19. Fang R, Zhao S, Hou P, et al. 3D interconnected electrode materials with ultrahigh areal sulfur loading for Li-S batteries. *Adv Mater* 2016;28:3374-82. DOI
20. Kong L, Peng HJ, Huang JQ, Zhang Q. Review of nanostructured current collectors in lithium-sulfur batteries. *Nano Res* 2017;10:4027-54. DOI
21. Li P, Ma L, Wu T, et al. Chemical immobilization and conversion of active polysulfides directly by copper current collector: a new approach to enabling stable room-temperature Li-S and Na-S batteries. *Adv Energy Mater* 2018;8:1800624. DOI
22. Zheng S, Han P, Han Z, Li P, Zhang H, Yang J. Nano-copper-assisted immobilization of sulfur in high-surface-area mesoporous

carbon cathodes for room temperature Na-S batteries. *Adv Energy Mater* 2014;4:1400226. DOI

23. Meng W, Dang Z, Li D, Jiang L, Fang D. Efficient sodium storage in selenium electrodes achieved by selenium doping and copper current collector induced displacement redox mechanisms. *Adv Funct Materials* 2022;32:2204364. DOI
24. Lu C, Li A, Li G, et al. S-decorated porous Ti_3C_2 MXene combined with in situ forming Cu_2Se as effective shuttling interrupter in Na-Se batteries. *Adv Mater* 2021;33:2008414. DOI
25. Zhou J, Yang Y, Zhang Y, et al. Sulfur in amorphous silica for an advanced room-temperature sodium-sulfur battery. *Angew Chem Int Ed Engl* 2021;60:10129-36. DOI
26. Zhu P, Gastol D, Marshall J, Sommerville R, Goodship V, Kendrick E. A review of current collectors for lithium-ion batteries. *J Power Sources* 2021;485:229321. DOI
27. Eng AYS, Kumar V, Zhang Y, et al. Room-temperature sodium-sulfur batteries and beyond: realizing practical high energy systems through anode, cathode, and electrolyte engineering. *Adv Energy Mater* 2021;11:2003493. DOI
28. Wang Y, Lai Y, Chu J, et al. Tunable electrocatalytic behavior of sodiated MoS_2 active sites toward efficient sulfur redox reactions in room-temperature Na-S batteries. *Adv Mater* 2021;33:2100229. DOI
29. Huang S, Fan S, Xie L, et al. Promoting highly reversible sodium storage of iron sulfide hollow polyhedrons via cobalt incorporation and graphene wrapping. *Adv Energy Mater* 2019;9:1901584. DOI
30. Li K, Zhang J, Lin D, et al. Evolution of the electrochemical interface in sodium ion batteries with ether electrolytes. *Nat Commun* 2019;10:725. DOI PubMed PMC
31. Li G, Wang S, Zhang YY, Li M, Chen ZW, Lu J. Revisiting the role of polysulfides in lithium-sulfur batteries. *Adv Mater* 2018;30:e1705590. DOI
32. Harks PPRML, Robledo CB, Verhallen TW, Notten PHL, Mulder FM. The significance of elemental sulfur dissolution in liquid electrolyte lithium sulfur batteries. *Adv Energy Mater* 2017;7:1601635. DOI
33. Liu H, Lai WH, Yang Q, et al. Understanding sulfur redox mechanisms in different electrolytes for room-temperature Na-S batteries. *Nanomicro Lett* 2021;13:121. DOI PubMed PMC
34. Yan D, Huang S, Von Lim Y, et al. Stepwise intercalation-conversion-intercalation sodiation mechanism in $CuInS_2$ prompting sodium storage performance. *ACS Energy Lett* 2020;5:3725-32. DOI
35. Liang W, Whangbo M. Conductivity anisotropy and structural phase transition in covellite CuS. *Solid State Commun* 1993;85:405-8. DOI
36. Perry DL, Taylor JA. X-ray photoelectron and auger spectroscopic studies of Cu_2S and CuS. *J Mater Sci Lett* 1986;5:384-6. DOI
37. Liu Y, Liu M, Swihart MT. Reversible crystal phase interconversion between covellite CuS and high chalcocite Cu_2S nanocrystals. *Chem Mater* 2017;29:4783-91. DOI
38. Fang Y, Yu XY, Lou XW. Bullet-like Cu_9S_5 hollow particles coated with nitrogen-doped carbon for sodium-ion batteries. *Angew Chem Int Ed Engl* 2019;58:7744-8. DOI
39. Li H, Wang Y, Jiang J, Zhang Y, Peng Y, Zhao J. CuS microspheres as high-performance anode material for na-ion batteries. *Electrochimica Acta* 2017;247:851-9. DOI
40. Song YX, Shi Y, Wan J, et al. Direct tracking of the polysulfide shuttling and interfacial evolution in all-solid-state lithium-sulfur batteries: a degradation mechanism study. *Energy Environ Sci* 2019;12:2496-506. DOI
41. Fang YJ, Luan DY, Chen Y, Gao SY, Lou XW. Rationally designed three-layered Cu_2S@Carbon@MoS_2 hierarchical nanoboxes for efficient sodium storage. *Angewandte Chemie* 2020;132:7245-50. DOI
42. Yamada M, Watanabe T, Gunji T, Wu J, Matsumoto F. Review of the design of current collectors for improving the battery performance in lithium-ion and post-lithium-ion batteries. *Electrochem* 2020;1:124-59. DOI
43. Wang T, Yang H, Lu B. Ultra-stable sodium ion battery cathode realized by Cu_7S_4 nanoparticles. *J Power Sources* 2018;399:105-14. DOI
44. Cao X, Lu Q, Xu X, Yan J, Zeng H. Single-crystal snowflake of Cu_7S_4: low temperature, large scale synthesis and growth mechanism. *Mater Lett* 2008;62:2567-70. DOI
45. Ye C, Jiao Y, Chao D, et al. Electron-state confinement of polysulfides for highly stable sodium-sulfur batteries. *Adv Mater* 2020;32:1907557. DOI
46. Yan Z, Liang Y, Hua W, et al. Multiregion Janus-featured cobalt phosphide-cobalt composite for highly reversible room-temperature sodium-sulfur batteries. *ACS Nano* 2020;14:10284-93. DOI
47. Huang S, Zhang L, Lu X, et al. Tunable pseudocapacitance in 3D $TiO_{2-\delta}$ nanomembranes enabling superior lithium storage performance. *ACS Nano* 2017;11:821-30. DOI
48. Huang S, Liu L, Zheng Y, et al. Efficient sodium storage in rolled-up amorphous Si nanomembranes. *Adv Mater* 2018;30:1706637. DOI